

# X-ray Emission of Baryonic Gas in the Universe: Luminosity-Temperature Relationship and Soft-Band Background

Tong-Jie Zhang<sup>1,2</sup>, Jiren Liu<sup>3</sup>, Long-long Feng<sup>3,5</sup>, Ping He<sup>4</sup>, Li-Zhi Fang<sup>2</sup>

## ABSTRACT

We study the X-ray emission of baryon fluid in the universe using the WIGEON cosmological hydrodynamic simulations. It has been revealed that cosmic baryon fluid in the nonlinear regime behaves like Burgers turbulence, i.e. the fluid field consists of shocks. Like turbulence in incompressible fluid, the Burgers turbulence plays an important role in converting the kinetic energy of the fluid to thermal energy and heats the gas. We show that the simulation sample of the  $\Lambda$ CDM model without adding extra heating sources can fit well the observed distributions of X-ray luminosity versus temperature ( $L_x$  vs.  $T$ ) of galaxy groups and is also consistent with the distributions of X-ray luminosity versus velocity dispersion ( $L_x$  vs.  $\sigma$ ). Because the baryonic gas is multiphase, the  $L_x - T$  and  $L_x - \sigma$  distributions are significantly scattered. If we describe the relationships by power laws  $L_x \propto T^{\alpha_{LT}}$  and  $L_x \propto \sigma^{\alpha_{LV}}$ , we find  $\alpha_{LT} > 2.5$  and  $\alpha_{LV} > 2.1$ . The X-ray background in the soft 0.5 – 2 keV band emitted by the baryonic gas in the temperature range  $10^5 < T < 10^7$  K has also been calculated. We show that of the total background, (1) no more than 2% comes from the region with temperature less than  $10^{6.5}$  K, and (2) no more than 7% is from the region of dark matter with mass density  $\rho_{dm} < 50\bar{\rho}_{dm}$ . The region of  $\rho_{dm} > 50\bar{\rho}_{dm}$  is generally clustered and discretely distributed. Therefore, almost all of the soft X-ray background comes from clustered sources, and the contribution from truly diffuse gas is probably negligible. This point agrees with current X-ray observations.

---

<sup>1</sup>Department of Astronomy, Beijing Normal University, Beijing 100875, China; tjzhang@bnu.edu.cn

<sup>2</sup>Department of Physics, University of Arizona, Tucson, AZ 85721; fanglz@physics.arizona.edu, tzhang@physics.arizona.edu

<sup>3</sup>Purple Mountain Observatory, Nanjing 210008, China; liujr@mail.ustc.edu.cn, fengll@pmo.ac.cn

<sup>4</sup>Institute of Theoretical Physics, Chinese Academy of Science, Beijing, P.R.China; hep@itp.ac.cn

<sup>5</sup>National Astronomical Observatories, Chinese Academy of Science, Chao-Yang District, Beijing 100012, China

*Subject headings:* cosmology: theory - large-scale structure of universe - X-rays: diffuse background - methods: numerical

## 1. Introduction

In the linear regime of gravitational clustering of cosmic matter, the evolution of baryonic gas follows dark matter point by point (Bi et al. 1992; Fang et al. 1993; Nusser & Haehnelt 1999; Nusser 2000). That is, the density and velocity distributions of baryonic matter can be obtained by a similar mapping from the dark matter field. The similar mapping has also been used in modeling the gas in clusters of galaxies (Kaiser 1986). However, it has been found that the similarity between the mass and velocity fields of baryonic gas and dark matter is broken in clusters that are formed through highly non-linear evolution. The mechanism of the breaking of similarity is due to the different dynamical behavior of dark matter and baryonic gas. The former is collisionless, while the latter is approximately an ideal fluid. The velocity field of collisionless dark matter particles is multivalued at the intersection of their trajectories, while baryon fluid always has a single-value velocity field. Thus, shocks in baryon fluid will appear at the intersection and break the similarity between the mass and velocity fields of baryon fluid and dark matter (Shandarin & Zel'dovich 1989).

At later times, it has been recognized that shocks occur not only in high-, but also in middle- and even low-density regions. This point has been shown by the dynamical equation of baryonic gas. Although cosmic baryonic gas is a Navier-Stokes fluid, its evolution is dominated by the growth mode, which is approximately governed by a random-force-driven Burgers equation, and the random force is produced by the gravity of the random field of dark matter (Gurbatov et al 1989; Berera & Fang 1994; Vergassola et al. 1994; Jones 1999; Matarrese and Mohayaee 2002; Pando et al. 2002, Pando et al 2004). When the Reynolds number is large, shock-caused turbulence, called Burgers turbulence, will develop in the fluid (Lässig 2000). The dynamics and thermodynamics of baryonic gas will be substantially affected by the Burgers turbulence. Dynamically, it will lead to the discrepancy between baryonic matter and dark matter, like the discrepancy of a passive substance from the underlying field during nonlinear evolution (e.g. Shraiman & Siggia 2000). Thermodynamically, the Burgers turbulence leads to the multiple phases of thermal properties and to converting the bulk kinetic energy of the fluid to thermal energy. For the system of cosmic baryonic and dark matter, a large Reynolds number actually corresponds to the onset of the non-linear regime of the gravitational clustering. Therefore, the similarity between baryonic and dark matter will inevitably break in the non-linear regime, and the dynamical

and thermodynamical effects of the Burgers turbulence must be considered.

Some effects of the Burgers turbulence have been detected with observational data and/or hydrodynamic simulation samples of cosmic baryonic gas. First, the statistical decoupling between the density and velocity fields of baryonic gas and dark matter is found to be significant on scales larger than the Jeans length (Pando et al 2004; Kim et al 2005). The importance of the discrepancy in the early nonlinear evolution has also been noted by Yoshida et al. (2003). Second, the transmitted flux of QSOs' Ly $\alpha$  absorption is found to be remarkably intermittent (Jamkhedkar et al 2000, 2003, 2005; Pando et al 2002; Feng et al 2003), which is consistent with the prediction of the intermittence of fully developed Burgers turbulence (Polyakov 1995; Balkovsky et al. 1997; Frisch et al 2001). Third, the temperature field of the baryonic gas is multiphase, and the heating caused by the shocks of the Burgers turbulence is substantial. Consequently, the distribution of the baryon fraction on large scales is nonuniform (He et al. 2005), and high-entropy gas is produced (He et al. 2004).

In this paper, we extend these studies to the X-ray emission of the hot baryonic gas in the universe. X-ray emission of galaxy groups is considered as important evidence of the similarity breaking between baryon fluid and dark matter. The relation between X-ray luminosity  $L_x$  and temperature  $T$  predicted by the similarity takes the form of a power law,  $L_x \propto T^\alpha$ , with an index of  $\alpha = 2$  (Kaiser 1991), while the observed result is  $\alpha > 2$  (Edge & Steward 1991; David et al. 1993; Wu et al 1999; Helsdon & Ponman 2000; Xue & Wu 2000; Croston et al. 2005). Moreover, the X-ray background in the soft band given by similarity is found to be much higher than the observed upper limit. In order to solve these problems, various models of non-gravitational heating for baryonic gas have been proposed (e.g. Valageas & Silk 1999; Tozzi & Norman 2001; Voit et al 2002; Zhang & Pen 2003; Xue & Wu 2003). The common goal of these models is to violate the similarity by heating baryonic gas before it falls into gravity potential wells. The amount of heating is of the order of 1 keV nucleon $^{-1}$  (Pen 1999; Wu et al 1999).

However, most non-gravitational heating models *assume* that the similarity will still hold without the non-gravitational heating sources. This point, as pointed out above, is actually inconsistent with the dynamics of the cosmic baryonic gas in the non-linear regime. Baryonic gas, either in high- or in low-density regions, will be heated when Burgers turbulence develops, regardless of whether non-gravitational heating is added. Typical shocks of the Burgers turbulence can convert the kinetic energy of a baryon fluid with a speed of a few hundred km s $^{-1}$  into thermal energy (He et al. 2004; Kim et al. 2005), which is of the order of 1 keV nucleon $^{-1}$ . Therefore, the thermodynamical effect of the Burgers turbulence should be substantial on the  $L_x - T$  relation and soft X-ray background. We need, at least,

to estimate the effect of the hydrodynamic heating on the X-ray emission before considering extra non-gravitational heating sources.

The paper is organized as follows. §2 describes the features of the baryonic gas as a Burgers fluid with samples of hydrodynamic cosmological simulation. §3 presents the analysis of the relationships between X-ray luminosity and mass density, temperature, and velocity dispersion. The soft X-ray background radiation is addressed in §4. Finally, the conclusions and discussion are given in §5.

## 2. Baryonic gas and Burgers turbulence

### 2.1. Gravitational clustering and Burgers fluid

The baryonic gas is generally assumed to be an ideal fluid satisfying the hydrodynamic equations

$$\frac{\partial \delta}{\partial t} + \frac{1}{a} \nabla \cdot (1 + \delta) \mathbf{v} = 0 \quad (1)$$

$$\frac{\partial a \mathbf{v}}{\partial t} + (\mathbf{v} \cdot \nabla) \mathbf{v} = -\frac{1}{\rho} \nabla p - \nabla \phi \quad (2)$$

$$\frac{\partial \mathcal{E}}{\partial t} + 5 \frac{\dot{a}}{a} \mathcal{E} + \frac{1}{a} \nabla \cdot (\mathcal{E} \mathbf{v}) = -\frac{1}{a} \nabla \cdot (p \mathbf{v}) - \frac{1}{a} \rho_{\text{igm}} \mathbf{v} \cdot \nabla \phi - \Lambda_{\text{rad}}, \quad (3)$$

where  $\rho$ ,  $\mathbf{v}$ ,  $\mathcal{E}$ , and  $p$  are the mass density, peculiar velocity, energy density, and pressure of the gas respectively. The cosmic factor  $a$  describes the cosmic expansion. The term  $\Lambda_{\text{rad}}$  in Eq.(3) is given by radiative heating and cooling of the baryonic gas per unit volume. The gravitational potential  $\phi$  in Eqs.(2) and (3) is given by

$$\nabla^2 \phi = 4\pi G a^2 \bar{\rho}_{\text{dm}} \delta_{\text{dm}}, \quad (4)$$

where  $\bar{\rho}_{\text{dm}}(t)$  and  $\delta_{\text{dm}}$  are, respectively, the mean mass density and density contrast of the perturbations of dark matter. Here we assume that the gravitational potential  $\phi$  is only produced by the dark matter mass perturbation.

During the process of gravitational clustering, there are two types of modes for the perturbations of the peculiar velocity field. For growth mode, the velocity field is curl-free, and the vertical mode is generally decaying with time. Therefore, one can define a velocity potential  $\varphi$  by  $v = -(1/a) \nabla \varphi$ . To sketch the gravitational clustering, we consider the case that all the thermal processes are approximated by the polytropic relations  $p \propto \rho^\gamma$ ,  $T \propto \rho^{\gamma-1}$ , or  $T = T_0(1+\delta)^{\gamma-1}$ , where  $\delta(\mathbf{x}, t) = [\rho(\mathbf{x}, t) - \bar{\rho}(t)]/\bar{\rho}(t)$  is the baryon mass density

perturbation. In this case, the equation of velocity potential, Eq.(3), can be approximately rewritten as

$$\frac{\partial \varphi}{\partial t} - \frac{1}{2a^2}(\nabla \varphi)^2 - \frac{\nu}{a^2}\nabla^2 \varphi = \phi, \quad (5)$$

where the coefficient  $\nu/a^2 = 1/k_J^2$  acts like a viscosity due to thermal diffusion and is characterized by the Jeans length  $k_J^2 = (a^2/t^2)(\mu m_p/\gamma k_B T_0)$ .

Eq.(5) is a stochastic-force-driven Burgers equation, which contains two scales: the dissipation length or the Jeans length  $1/k_J$  and the correlation length of the gravity potential  $\phi, r_c$ . The intensity of  $\phi$  can be quantified by the density contrast of dark matter  $\delta_{dm}$ . A basic feature of the Burgers equation is that turbulence will develop in the fluid if the following condition holds (e.g. Feng et al 2003):

$$(k_J r_c)^{2/3} \langle \delta_{dm}^2 \rangle^{1/3} > 1, \quad (6)$$

which corresponds to the condition that the Reynolds number must be larger than 1 for the turbulence of incompressible fluid. Therefore, the quantity on the left-hand side of Eq.(6) plays the same role as the Reynolds number in the original fluid (Lässig 2000).

Burgers turbulence is qualitatively different from the turbulence of incompressible fluid. The latter generally consists of vortices on various scales, while the former is a collection of shocks. These features arise because, for growth modes, the fluid is potential and the velocity field is irrotational. If  $\nu \rightarrow 0$ , the velocity field in the Burgers prescription acquires singularities due to the discontinuities caused by strong shocks. The nonlinear feature of the velocity field of baryonic gas can be understood as a field consisting of these shocks.

## 2.2. Samples of hydrodynamic simulation

In the numerical calculation, we still use the hydrodynamic equations (1)-(3) to model the baryonic gas, because the decaying modes will disappear automatically, and the result is just on the growth modes. Since the field of baryonic gas in the nonlinear regime consists of strong and weak shocks, the hydrodynamic cosmological simulation should be able to capture shocks and calculate the thermal properties of the baryon fluid in front of and behind shocks. Therefore, an optimal simulation scheme has to satisfy two conditions: (1) it is effective in capturing shock and discontinuity transitions, and (2) it accurately calculates piecewise smooth functions with a high resolution. Condition (1) is obvious in studying a field consisting of shocks. Condition (2) is important in calculating the shock heating, which depends on the difference between gaseous dynamical and thermal properties of pre- and postshock regions.

We take the WIGEON (Weno for Intergalactic medium and Galaxy Evolution and formatiON) code (Feng et al. 2004), which is a cosmological hydrodynamic/ $N$ -body code based on the Weighted Essentially Non-Oscillatory (WENO) algorithm (Harten et al. 1986; Liu et al. 1994; Jiang & Shu 1996; Shu 1998; Fedkiw, Sapiro & Shu 2003; Shu 2003). The WENO algorithm is an Eulerian approach. It has been applied to hydrodynamic problems containing strong shocks, complex structures, and turbulence. It has also been applied to the Burgers equation (Shu 1999). The WIGEON code has passed the necessary tests including the Sedov blast wave and the formation of the Zel'dovich pancake (Feng et al. 2004). It is successful in showing the features of the Burgers fluid with the velocity field of cosmic baryonic gas. That is, when the Reynolds number is high, the velocity field consists of an ensemble of shocks with the following features: (1) the probability distribution function (PDF) of velocity is asymmetric between acceleration and deceleration events and (2) the PDF of velocity difference  $\Delta v = v(x + r) - v(x)$  satisfies the scaling relation for a Burgers fluid (Kim et al. 2005; He et al. 2005).

In order to accurately calculate the shock heating, the resolution of the simulation should be less than the thickness of the shock, which is of the order of the Jeans diffusion, which is greater than  $0.2 h^{-1}$  Mpc for redshifts  $z < 2$  (Bi et al. 2003). On scales less than the Jeans diffusion, shock-caused discontinuity is small, and the heating effect is weak. We perform three sets of simulations: two (samples A and B) are in a periodic cubic box with a size of  $100 h^{-1}$  Mpc, a  $512^3$  grid and an equal number of dark matter particles, and another one (sample C) is in a cubic box with a size of  $25 h^{-1}$  Mpc, a  $192^3$  grid and an equal number of dark matter particles. The sizes of the grids are  $100/512 = 0.20$  and  $25/192 = 0.13 h^{-1}$  Mpc, respectively. Sample C is the same as that used in the analysis of the Burgers fluid features of cosmic baryonic gas (Pando et al 2004; Kim et al 2005).

We use the standard  $\Lambda$ CDM model, which is specified by the matter density parameter  $\Omega_m = 0.27$ , baryonic matter density parameter  $\Omega_b = 0.044$ , cosmological constant  $\Omega_\Lambda = 0.73$ , Hubble constant  $h = 0.71$ , and mass fluctuation  $\sigma_8 = 0.84$  within a sphere of radius  $8 h^{-1}$  Mpc. The transfer function is calculated using CMBFAST (Seljak & Zaldarriaga 1996). For sample C, we use the same parameters but  $\Omega_b = 0.026$ . We use the cloud-in-cell method for mass assignment and interpolation and adopt the seven-point finite difference to approximate the Laplacian operator. The simulations start at the redshift  $z = 49$ , and the results output at redshifts  $z=2, 1, 0.5$ , and 0.

For the two simulations of the  $100 h^{-1}$  Mpc cubic box, one considered the metal abundance (sample A), and one used the primordial composition (sample B). For sample C, we used the primordial composition, for which the atomic process of H and He ( $X=0.76, Y=0.24$ ) is calculated as in Theuns et al. (1998). For sample A, the metal cooling and metal line

emission is calculated by the phenomenological method (1) assuming a uniform evolving metallicity  $Z = 0.3Z_{\odot}(t/t_0)$ , where  $t_0$  is the present universe age, and (2) computing the cooling function using the table of Sutherland & Dopita (1993). An evolving background UV spectrum calculated by Haardt & Madau (1996) is used. With the comparison among samples A, B, and C, one can estimate the effects of the size of the simulation box and the metal abundance.

A common problem of hydrodynamic simulation with Eulerian variables is that it cannot describe compact objects on scales less than the size of the grid. Therefore, we do not use these samples to study rich clusters. On the other hand, the samples with Eulerian variables make it easy to reach low-density regions. They are suitable for analyzing X-ray emission of baryonic gas from background and weakly clustered structures, such as groups.

### 2.3. Shock heating and similarity breaking

Shock heating is well known in the heating problem of groups, clusters (Cavaliere et al 1997), and large-scale structures (Miniati et al 2004; Kang et al. 2004). The scenario of Burgers turbulence shows that, in nonlinear regime, shocks or complex structures of the velocity field form around massive halos, as well as regions with moderate and even low mass density. Therefore, it heats the gas in various density fields. Figure 1 presents the relations between the temperature and mass density of baryonic gas at redshifts  $z = 2, 1, 0.5$ , and  $0.0$ . Each panel contains 19,200 data points randomly drawn from sample C. Figure 1 shows that the gas is multiphase. It contains the phase of tightly correlated  $T$  and  $\rho$  in the region of  $T \leq 10^{4.5}\text{K}$  and  $0.01 < \rho_{\text{igm}} < 2$  and also a phase of the scattered distribution of  $T$  ( $> 10^5\text{K}$ ) with respect to a given  $\rho$ . Comparing with other numerical simulation results (e.g., Ryu et al. 1993; Katz, Weinberg, & Hernquist 1996; Theuns et al. 1998; Davé et al. 1999; Valageas, Schaeffer, Silk 2002; Springel & Hernquist 2002), the shock-heated gas is more significant in the moderate- and low-density ( $\rho_{\text{igm}} \simeq 1$ ) regions. This is because the WENO code is effective in capturing shocks in both high- and low-density regions.

A dynamical effect of the Burgers turbulence is the discrepancy between the fields of baryonic gas and dark matter. Figure 2 shows two-dimensional contours of the baryonic gas density  $\rho_{\text{igm}}$  and dark matter density  $\rho_{\text{dm}}$ , both of which are in units of their corresponding average density  $\bar{\rho}_{\text{igm}}$  and  $\bar{\rho}_{\text{dm}}$ . One can clearly see from Figure 2 that the density of baryonic gas (*right*) is not simply proportional to that of dark matter (*left*). The size of the over-density region  $\rho_{\text{igm}} > 1$  is generally larger than the dark matter counterpart. Therefore, the clumping of baryonic gas is generally weaker than that of dark matter.

Figure 3 shows the same slice as in Figure 2, but gives the two-dimensional contours of temperature and the ratio between the densities of baryonic matter and dark matter. The left panel shows that the contours of  $\rho_{\text{igm}}/\rho_{\text{dm}} > 1$  are located outside the massive halos. Contrarily, the center of the halos has only a low baryon fraction  $\rho_{\text{igm}}/\rho_{\text{dm}} < 1$ . It is more interesting to see from the right panel that the shape of high-temperature regions is very different from high-density regions of either dark matter or baryonic matter. In Figure 3, the high-density regions of  $\rho_{\text{igm}}$  or  $\rho_{\text{dm}}$  consist of filaments and knots, while the high-temperature regions are isolated spots. Therefore, temperature is not simply proportional to  $\rho_{\text{igm}}$  or  $\rho_{\text{dm}}$ , but multiphase.

In summary, with respect to the similarity model, the non-linear evolution of cosmic baryon fluid leads to (1) a shallower distribution of baryonic gas, (2) a lower density  $\rho_{\text{igm}}$  inside the dark matter halo, and (3) a higher temperature outside dark matter halos. Generally, various non-gravitational heating models try to realize the above-mentioned features. Figures 1-3 show, however, that all of these features are naturally yielded when baryonic gas is undergoing a Burgers turbulence evolution.

### 3. X-ray emission of baryonic gas from groups of galaxies

#### 3.1. Relationship between X-ray luminosity and mass density

For the baryonic gas in each cell of the grid with temperature  $T > 10^5$  K, we can calculate the X-ray luminosity by the bremsstrahlung process assuming that all H and He atoms are ionized, and then obtain a field of luminosity  $L_x$ . In Figure 4, we plot, respectively, the relationships between the X-ray luminosity and mass density of baryonic gas at redshifts  $z=0.0, 0.5, 1.0$ , and  $2$ , which are given by 9931, 9119, 7314, and 4864 data points randomly selected from sample C. Here we consider only the bremsstrahlung radiative process, without considering the effect of metal line emission, which may lead to an uncertainty of no more than about 20%.

Figure 4 shows that for  $z < 2$ , the  $L_x - \rho_{\text{igm}}$  distribution is weakly dependent on redshift, and X-ray luminosity is correlated with the density  $\rho_{\text{igm}}$ . Considering the adiabatic “equation of state”  $T \propto \rho^{2/3}$  (e.g. He et al 2004), we then obtain  $L_x \propto \rho_{\text{igm}}^2 T^{1/2} \propto \rho^{2.3}$ . However, the  $L_x - \rho_{\text{igm}}$  distribution is actually scattered due to the multiphase property of baryonic gas. For a given  $\rho_{\text{igm}}$ , the scatter of baryonic gas temperature is of the order of  $10^3$ , i.e. from  $10^5$  to  $10^7$  K. Therefore, the scatter of  $L_x$  for a given  $\rho_{\text{igm}}$  can be as large as a factor of  $10^{1.5}$ .

Table 1 gives the mean X-ray luminosity for sample C from regions with temperature  $10^6 < T < 10^7$  K and dark matter density  $\rho_{\text{dm}} < 100, 50$ , and  $10$ . It shows that the X-ray

luminosity is mostly produced from the epoch of  $z \leq 1$ . At  $z = 1$ , about 25% of the X-ray emission is from moderate and low clustering regions  $\rho_{\text{dm}} < 50$ , while at  $z = 0$ , only about 10% is from moderate- and low-clustering areas.

Figure 5 presents the  $L_{\text{x}} - \rho_{\text{dm}}$  relationship for the  $z = 0$  sample, but the fields of  $\rho_{\text{dm}}$  and  $T$  are decomposed to the cells on scales of  $0.52, 1.04$ , and  $2.08 \text{ } h^{-1} \text{ Mpc}$ . We use the scaling function of the discrete wavelet transform (DWT) to perform the decomposition. The DWT decomposition does not cause false correlation (Fang & Thews 1998). Therefore,  $L_{\text{x}}$  of Figure 5 is the total luminosity from the cells on scales of  $0.52, 1.04$ , and  $2.08 \text{ } h^{-1} \text{ Mpc}$ , and  $\rho_{\text{dm}}$  is the mean density of dark matter in these cells.

The cells on scales of  $0.52, 1.04$ , and  $2.08 \text{ } h^{-1} \text{ Mpc}$  with density  $\rho_{\text{dm}} > 50$  have total masses  $\geq 0.27, 2.18$ , and  $17.4 \times 10^{12} \text{ } M_{\odot}$ , respectively. These masses and sizes correspond to groups or clusters. It has been shown that the DWT-identified cells on scale of  $1.5 \text{ } h^{-1} \text{ Mpc}$  with high density are statistically the same as clusters identified by a traditional method, such as the friends-of-friends algorithm (Xu et al. 1998). Moreover, the cells with high density are found to be virialized or quasi-virialized (Xu et al 2000). Therefore, the DWT-identified cells with  $\rho_{\text{dm}} \geq 50$  on a scale of  $1.04 \text{ } h^{-1} \text{ Mpc}$  or  $\rho_{\text{dm}} \geq 100$  on a scale of  $0.52 \text{ } h^{-1} \text{ Mpc}$  give an ensemble of groups and clusters. This can be applied to estimate the statistical properties of galaxy groups. The cells with high  $L_{\text{x}}$  simulate the behavior of the X-ray emission of galaxy groups.

Generally, the mean of the luminosity  $L_{\text{x}}$  of Figure 5 becomes larger with the increase of the cell scale. This is trivial, because the volume of a  $1.04$  ( $2.08$ )  $\text{ } h^{-1} \text{ Mpc}$  cell is 8 times larger than that of a  $0.52$  ( $1.04$ )  $\text{ } h^{-1} \text{ Mpc}$  cell, and so on. An interesting feature shown in Figure 5 is that the scatter of the  $L_{\text{x}} - T$  distributions does not reduce with the increase of cell scale, even when the smoothing scale of  $2.08 \text{ } h^{-1} \text{ Mpc}$  is larger than the largest size of virialized collapsed objects. Therefore, the scatter of luminosity should be not only from collapse, but dependent on the multiphase property of the temperature field of baryonic gas.

Table 1. Mean intensity of X-ray luminosity ( $10^6 < T < 10^7 \text{ K}$ )

| redshift  | total                 | $\rho_{\text{dm}} < 100$<br>(in unit of $10^{43} \text{ ergs s}^{-1}$ ) | $\rho_{\text{dm}} < 50$ | $\rho_{\text{dm}} < 10$ |
|-----------|-----------------------|---|-------------------------|-------------------------|
| $z = 2.0$ | $9.10 \times 10^{-8}$ | $4.12 \times 10^{-8}$   | $2.69 \times 10^{-8}$   | $5.39 \times 10^{-9}$   |
| $z = 1.0$ | $1.12 \times 10^{-7}$ | $4.41 \times 10^{-8}$   | $2.77 \times 10^{-8}$   | $5.04 \times 10^{-9}$   |
| $z = 0.0$ | $2.74 \times 10^{-7}$ | $5.27 \times 10^{-8}$   | $3.28 \times 10^{-8}$   | $5.63 \times 10^{-9}$   |

### 3.2. Relationship between X-ray luminosity and temperature

Figure 6 presents the distribution of  $L_x$  versus  $T$  for the simulation sample A at  $z = 0$  on a scale of  $0.78 h^{-1}$  Mpc. The observed  $L_x - T$  distribution of galaxy groups is also shown in Figure 6. The data are taken from Helsdon & Ponman (2000), Xue & Wu (2000), and Croston et al (2005). The three observed samples are partially overlapped. If a group is listed in two or three samples, we only use the data of the latest one.

Figure 6 shows that the simulated results are in good agreement with the observed  $L_x - T$  distribution of groups. First, the simulated points of high  $L_x$  and  $T$  are located in the same areas as in the observed  $L_x - T$  distribution. As mentioned in §3.1 above, the high  $L_x$  cells are virialized or quasi-virialized objects with masses of groups. Second, the observed  $L_x - T$  distribution is connected smoothly and continuously with simulation points with lower  $L_x$  and  $T$ . The cells with lower  $L_x$  have lower density  $\rho_{\text{igm}}$  or  $\rho_{\text{dm}}$ . Therefore, Figure 6 strongly indicates that the X-ray emission from baryonic gas related to groups underwent the same dynamical and thermodynamical evolution as that of the diffuse clouds, which have weaker X-ray emission than groups.

Similar to the distribution of  $L_x$  versus  $\rho_{\text{igm}}$  and  $\rho_{\text{dm}}$  (Figures 4 and 5), the  $L_x - T$  distribution is largely scattered. This scatter cannot be explained by the Jeans diffusion or another Gaussian noise process. Figure 6 shows an upper envelope in the  $L_x - T$  distributions, which corresponds to the maximum gas density  $\rho_{\text{igm}}$  for a given temperature  $T$ . The upper envelope can be approximately fitted by a power law  $L_x \propto T^{2.5}$ . Thus, we can conclude that if we try to fit the  $L_x - T$  relationship of groups by a power law  $L_x \propto T^{\alpha_{LT}}$ , the index  $\alpha_{LT}$  should be  $\geq 2.5$ . This result is consistent with the measured  $\alpha_{LT}$  for samples of groups, which are  $3.6 < \alpha < 8.2$  (Helsdon & Ponman 2000),  $2.1 < \alpha < 5.7$  (Xue & Wu 2000), and  $2.7 < \alpha < 4.1$  (Croston et al. 2005).

Figure 7 is the same as Figure 6, but for sample C. The DWT variables are on scales of  $0.52$  and  $1.04 h^{-1}$  Mpc. The simulation data in Figure 7 are also basically consistent with the observed result. Therefore, the effect of metal cooling on the  $L_x - T$  relation is small. As we know, the major effect of the metal cooling is to form a condensation branch in the temperature-density distribution. The temperature of the condensation branch is low, and therefore, these are not strong X-ray sources. It is interesting to see that Figure 7 shows a lower envelope with a power law  $L_x \propto T^{-5}$ . This power law is about the same as  $L_x \propto T^{-4.8}$  given by the hydrodynamic simulation of Davé et al (2002). However, our result of the  $L_x - T$  distribution is scattered, i.e. fills in the range between the lower and upper envelopes. Observed samples also show the scatter and are consistent with our simulation sample.

Figure 8 presents the  $L_x - T$  distribution for sample C, but decomposed on physical scales of  $0.69 h^{-1}$  Mpc at redshift  $z = 0.5$  and  $0.5 h^{-1}$  Mpc at  $z = 1$ . The observed points are the same as those in Figures 6 and 7. We see that the simulated  $L_x - T$  distribution is almost  $z$  independent in the range  $z \leq 1$ . This is consistent with a weak evolution scenario of temperature and entropy fields in the range  $z \leq 2$  (He et al. 2004). Thus, we may predict that the  $L_x - T$  distribution of groups at  $z \sim 1$  should not be very different from  $z = 0$ .

### 3.3. Relationship between X-ray luminosity and velocity dispersion

The velocity dispersion in a cell can be estimated by the peculiar velocity difference within this cell. We use the DWT variables to calculate the velocity dispersion. The details of this algorithm are given by Yang et al (2001) and Kim et al. (2005). This method is effective in estimating the velocity dispersion of both virialized systems and quasi-virialized systems (Xu et al. 2000).

Figure 9 plots the distribution of X-ray luminosity  $L_x$  versus velocity dispersion of dark matter  $\sigma_{dm}$  for simulation sample C decomposed in cells on a scale of  $1.04 h^{-1}$  Mpc. The observed  $L_x - \sigma$  points of Mulchaey & Zabludoff (1998) are also shown in Figure 9. Many objects in this sample are actually rich clusters, which are outside of the simulated data points. Nevertheless, the observed points with low  $L_x$  and  $\sigma$  are clearly support to the simulated result.

The distribution of  $L_x$  versus  $\sigma_{dm}$  in Figure 9 is also substantially scattered. However, it does not have a very clear upper envelopes but one can still see a less clear upper envelop, which can be roughly fitted by a power law  $L_x \propto \sigma^{2.1}$ . That is, if we try to describe the scattered  $L_x - \sigma$  distribution by a power law  $L_x \propto \sigma^{\alpha_{LV}}$ , the index  $\alpha_{LV}$  should be larger than 2.1. This is consistent with observational results  $\alpha_{LV} > 2.3$  (Helsdon & Ponman 2000; Xue & Wu 2000). The large scatter of  $L_x$  versus  $\sigma$  is caused by the large scatter of velocity versus density of both baryonic matter and dark matter.

## 4. Soft X-ray background

### 4.1. Mean and PDF of soft X-ray background

As the hot gas with high temperature ( $T > 10^7$ K) is always identified as clusters, we calculate the X-ray background intensity only from baryonic gas with temperature  $10^5 - 10^7$ K,

which is given by an integral

$$F(\nu_0) = \frac{1}{4\pi} \frac{c}{H_0} \int_0^{z_r} \epsilon([1+z]\nu_0, z) \frac{dz}{(1+z)^4 [\Omega_m(1+z)^3 + \Omega_\Lambda]^{1/2}}, \quad (7)$$

where  $F(\nu_0)$  is in units of  $\text{ergs s}^{-1} \text{cm}^{-2} \text{Hz}^{-1} \text{sr}^{-1}$  and  $\epsilon(\nu_0, z)$  is the volume emissivity of X-ray photons with local frequency  $\nu_0$  at redshift  $z$ . The emissivity  $\epsilon(\nu_0, z)$  is calculated using Raymond-Smith model (Raymond & Smith 1977). In the calculation of the X-ray background intensity, both the samples with and without metal cooling are considered.

The soft X-ray background mostly comes from hot clouds at  $z < 2$ . It is sufficient to produce maps by taking the integral of Eq.(7) from  $z = 0$  to 6. The algorithm of mapping is as follows. The simulation data are output every time when light crosses the simulation box with a size of  $100 \text{ h}^{-1} \text{Mpc}$ . For each output, we take the integral in Eq.(7) along one random chosen axis and produce a map of X-ray flux  $F$  at the redshift  $z$  of that box. After the simulation reaches  $z = 0$ , we have 60 maps of  $F$  at redshifts corresponding to a comoving distance at  $n \times 100 \text{ h}^{-1} \text{Mpc}$ , where  $n = 0, \dots, 59$ . One map of the background can then be obtained by (1) arranging a set of 60 two-dimensional maps with a randomized center, (2) taking a constant angular projection for each map, and (3) superposing the contributions of the 60 maps.

A typical two-dimensional map of the soft X-ray background from regions with  $10^5 < T < 10^7 \text{ K}$  based on sample A is shown in Figure 10. The angular size of the map is  $1^\circ \times 1^\circ$ , and its angular resolution is  $0'.06$ . Figure 11 gives the corresponding PDF of the intensity of the X-ray background in the band  $0.5 - 2 \text{ keV}$ . For sample A, the mean X-ray background intensity is  $(1.87 \pm 0.63) \times 10^{-12} \text{ ergs s}^{-1} \text{cm}^{-2} \text{deg}^{-2}$ , where the  $1\sigma$  error is from the variance of 50 two-dimensional maps. For sample B, we have  $(1.73 \pm 0.63) \times 10^{-12} \text{ ergs s}^{-1}$ . Therefore, the effect of metal cooling has to be less than 10%.

Table 2. Mean intensity of soft-band X-ray background

| $\rho_{\text{dm}}$<br>( $10^5 < T < 10^7 \text{ K}$ ) | Mean intensity ( $\text{ergs s}^{-1} \text{cm}^{-2} \text{deg}^{-2}$ ) |                                 |
|---|--|---------------------------------|
|   | Primordial abundance   | Metal abundance                 |
| total   | $1.73 \pm 0.63 \times 10^{-12}$  | $1.87 \pm 0.63 \times 10^{-12}$ |
| $\rho_{\text{dm}} < 100$                              | $2.90 \pm 0.62 \times 10^{-13}$  | $2.86 \pm 0.86 \times 10^{-13}$ |
| $\rho_{\text{dm}} < 50$                               | $1.27 \pm 0.29 \times 10^{-13}$  | $1.23 \pm 0.38 \times 10^{-13}$ |
| $\rho_{\text{dm}} < 10$                               | $1.55 \pm 0.41 \times 10^{-14}$  | $1.52 \pm 0.63 \times 10^{-14}$ |

## 4.2. Density dependence of soft-band X-ray background

It is usually believed that most X-ray background is attributed to resolvable discrete X-ray sources, such as active galactic nuclei (AGNs) and truly diffuse extragalactic baryonic clouds. As shown in §3, the dynamical and thermodynamical properties of baryonic clouds are continuously varying from low-density (diffuse) regions to high-density regions (collapsed and virialized objects). There is no clear criterion to distinguish the X-ray emission of truly diffuse baryonic gas from that of resolvable sources. We study this problem with the density dependence of the soft X-ray background.

We integrate Eq.(7), but only calculate X-ray emission from baryonic clouds with temperatures  $10^5 < T < 10^7$  K and in regions with  $\rho_{\text{dm}} < 100$ , 50, and 10. The results for sample A are shown in Figure 12, which contains three  $1^\circ \times 1^\circ$  maps corresponding to  $\rho_{\text{dm}} < 100$ , 50, and 10. The mean intensities of the soft-band X-ray background are listed in Table 2. We can see that less than 17% (7%) of the total soft X-ray background of  $10^5 < T < 10^7$  comes from clouds located in regions of dark matter with density contrast  $\rho_{\text{dm}} < 100$  (50). As mentioned in §3.2, the cells having  $\rho_{\text{dm}} > 100$  or  $> 50$  generally contain collapsed and virialized structures. From Figure 2 we can also see that the structures with  $\rho_{\text{dm}} > 100$  or 50 have only a very small volume fraction. These regions are discretely distributed. Therefore, they should be resolvable. Thus, one can conclude that the contribution of *truly* diffuse baryonic gas to the soft-band X-ray background is no more than about  $2.90 \times 10^{-13}$  ergs s $^{-1}$  cm $^{-2}$  deg $^{-2}$ . This result can also be seen from Table 1. Using data of the *XMM-Newton* Lockman Hole observation, Worsley et al (2005) show that in the soft-band (<2 keV), more than 90% of the X-ray background can be resolved. This result is consistent with Table 2. The simulation done by Croft et al (2001) found the X-ray background of the warm-hot intergalactic medium (WHIM) to be  $4.15 \times 10^{13}$  ergs s $^{-1}$  cm $^{-2}$  deg $^{-2}$ . This is a little larger than our result. This difference is probably attributable to the powerful shock-capturing ability of the WENO code.

It is also interesting to note from Table 2 that for the case of the total region, the sample considering the metal abundance (sample A) has a slightly higher mean intensity of the soft X-ray background than that without metal cooling (sample B), while for all other cases ( $\rho_{\text{dm}} < 100$ ) sample A gives a slightly lower mean intensity than that of the primordial abundance. This is because metal cooling can weaken the turbulence heating. The gas with metal cooling easily falls into gravity wells ( $\rho_{\text{dm}} > 100$ ). On the other hand, in the case of no metal cooling more gas will remain in less clustered regions and give higher X-ray emission from clouds with  $\rho_{\text{dm}} < 100$ . In all cases, the difference between samples A and B is small. Thus, the thermodynamical effect of metal cooling is much less the turbulence heating.

### 4.3. Temperature dependence of soft X-ray background

Similarly, we study the temperature dependence of soft X-ray background. We do the integral in Eq.(7), but only calculate X-ray emissions from baryonic clouds with temperatures less than  $10^{6.5}$  K. A  $1^\circ \times 1^\circ$  map of the soft X-ray background from clouds of  $T < 10^{6.5}$  of sample A is shown in Figure 13, and the corresponding PDF of the intensity of the X-ray background is given in Figure 14. The mean intensity is  $(9.38 \pm 3.06) \times 10^{-14}$  ergs s $^{-1}$  cm $^{-2}$  deg $^{-2}$  for sample A and  $(8.0 \pm 2.03) \times 10^{-14}$  ergs s $^{-1}$  cm $^{-2}$  deg $^{-2}$  for sample B. Therefore, no more than 5% of the total soft X-ray background of  $10^5 < T < 10^7$  K comes from clouds with temperature  $T < 10^{6.5}$  K. Most of soft X-ray background is attributed to baryonic clouds with high temperature ( $T > 10^{6.5}$ ).

## 5. Discussion and conclusions

The evolution of baryonic gas can be roughly divided into three stages. The first is the linear stage. It can be simply described by the similarity between the baryonic and dark matter. When the non-linear evolution takes place, Burgers turbulence develops. Baryonic gas will decouple with dark matter, and becomes multiphase. The kinetic energy of baryon fluid will be dissipated by the shocks of turbulence. Some cosmic baryonic gas finally falls into massive halos and evolves in the thermal equilibrium state in gravity wells. Some heated baryonic gas remains outside of gravity wells. The Burgers turbulence heating is not uniform. A uniform heating would contradict with the Ly $\alpha$  forest, which is produced by hydrogen clouds with a temperature of about  $10^4$ - $10^5$  K. Therefore, baryonic gas undergoing the Burgers turbulence evolution must be multiphase. In the stage of the Burgers turbulence, the dominant component in volume fraction is the gas in the low-temperature phase (He et al. 2004).

We show that the X-ray emission of baryonic gas can be well modeled by the above-mentioned scenario. That is, the observed distributions of  $L_x$  versus  $T$  and  $L_x$  versus  $\sigma$  of galaxy groups can be reproduced by the simulation sample of the  $\Lambda$ CDM model without adding extra heating sources. We also find that almost all of the soft-band X-ray background radiation is from clustered regions, and the contribution of diffuse gas with  $\rho_{\text{dm}} < 50$  is negligible. This is also consistent with current X-ray observations. These results show that the Burgers turbulence heating alone seems to be enough to account for the basic features of X-ray emission of baryonic gas in the universe.

We should also point out that star formation and its feedback on the baryonic gas are not considered in our simulation. Roughly, there are two types of feedback: (1) photoionization

heating by the UV emission of stars and AGNs and (2) injection of hot gas and energy by supernova explosions, or other sources of cosmic rays. Actually, the photoionization heating can be properly considered, if the UV background is adjusted by fitting the simulation with the observed mean flux decrement of QSOs' Ly $\alpha$  absorption spectrum (Feng et al. 2003). The significant effect of injecting hot gas and energy by supernovae is mostly on dwarf galaxies. Recent Ly $\alpha$  observations of protoclusters (Adelberger et al. 2003) suggest that AGN heating does not drastically affect the gas in clusters. Therefore, this heating mechanism may not be strong enough to change the basic features of the multiphase scenario given in this paper. Moreover, the shocks may lead to the electron temperature  $T_e$  being lower than the ion temperature  $T_i$ . Since the mean of the ratio  $T_i/T_e$  is generally less than 3 (Fox & Loeb 1997; Takizawa 1998; Yoshida et al. 2005), this effect may lead to an uncertainty of the luminosity  $L_x$  that is less than a factor of 2. Therefore, all conclusions should basically be held.

We thank the anonymous referees for many valuable suggestions. T.-J.Z. is supported by the Fellowship of the World Laboratory and thanks Peng-Jie Zhang for useful discussion and Ue-Li Pen for help. J.-R.L. is appreciative of Hy Trac for giving the parallel gravitation solver code and Cheng Ling-Mei for help on the Raymond-Smith model. T.-J.Z., L.-L.F. and P.H. acknowledge support from the National Science Foundation of China (grants 10473002, 10533010, 10573036 and 10545002). This work was also partially supported by US NSF AST 05-07340.

## REFERENCES

- Adelberger, K.L., et al. 2003, ApJ, 584, 45
- Balkovsky, E., Falkovich, G., Kolokolov, I., & Lebedev, V. 1997, Phys. Rev. Letts. 78, 1452
- Berera, A., & Fang, L.Z. 1994, Phys. Rev. Lett., 72, 458
- Bi, H.G., Börner, G., & Chu, Y.Q. 1992, A&A, 266, 1
- Bi, H., Fang, L.Z., Feng, L.L., & Jing, Y. 2003, ApJ, 598, 1
- Cavaliere, A., Menci, N., Tozzi, P., 1997, ApJ, 484, 21
- Cen, R. 1992, ApJS, 78, 341
- Croft, R.A.C., et al. 2001, ApJ, 557, 67
- Croston, J. H., Hardcastle, M. J., & Birkinshaw, M. 2005, MNRAS, 357, 279
- Davé, R., Hernquist, L., Katz, N. & Weinberg, D. H., 1999, ApJ, 511, 521
- Davé, R., Katz, N. & Weinberg, D. H., 2002, ApJ, 579, 23
- David, L. P., et al. 1993, ApJ, 412, 479
- Edge, A. C., & Stewart, G. C. 1991, MNRAS, 252, 428
- Fang, L.Z., Bi, H.G., Xiang, S.P., & Börner, G. 1993, ApJ, 413, 477
- Fang, L.Z., & Thews, R. 1998, *Wavelet in Physics*, (World Scientific, Singapore)
- Fedkiw, R.P., Sapiro, G., & Shu, C.W. 2003, J. Comput. Phys., 185, 309
- Feng, L.L., Pando, J., & Fang, L.Z. 2003, ApJ, 587, 478
- Feng, L.L., Shu, C.W., & Zhang, M. 2004, ApJ, 612, 1
- Fox, D.C., Loeb, A., 1997, ApJ, 491, 459
- Frisch, U., Bec, J., & Villone, B. 2001, Physica D, 152-153 620
- Gurbatov, S.N., Saichev, A.I., & Shandarin, S.F. 1989, MNRAS, 236, 385
- Haardt, F., & Madau, P. 1996, ApJ, 461, 20
- Harten, A., Osher, S., Engquist, B., & Chakravarthy, S. 1986, Appl. Numerical Math., 2, 347
- He, P., Feng, L.L., & Fang, L.Z. 2004, ApJ, 612, 14
- He, P., Feng, L.L., & Fang, L.Z. 2005, ApJ, 628, 14
- Helsdon, S. F., & Ponman, T. J. 2000, MNRAS, 315, 356

- Jamkhedkar, P., Feng, L.L., Zheng, W., Kirkman, D., Tytler, D., & Fang, L.Z. 2003 MNRAS, 343, 1110
- Jamkhedkar, P., Zhan, H., & Fang, L.Z. 2000, ApJ, 543, L1
- Jamkhedkar, P., Feng, L.L., Zheng, W., & Fang, L.Z. ApJ, in press (astro-ph/0507561)
- Jiang, G. & Shu, C.W. 1996, J. Comput. Phys., 126, 202
- Jones, B.T. 1999, MNRAS, 307, 376
- Kaiser, N. 1986, MNRAS, 222, 323
- Kaiser, N. 1991, ApJ, 383, 104
- Kang, H., Jones, T. W., 2004, Journal of the Korean Astronomical Society, 37, 405
- Katz, N., Weinberg, D. H., Hernquist, L., 1996, ApJS, 105, 19
- Kim, B., He, P., Pando, J., Feng, L.L., & Fang, L.Z. 2005, ApJ, 625, 599
- Lässig, M. 2000, Phys. Rev. Lett., 84, 2618
- Liu, X.D., Osher, S., & Chan, T. 1994, J. Comput. Phys., 115, 200
- Matarrese, S., & Mohayaee, R. 2002, MNRAS, 329, 37
- Miniati, F., Ferrara, A., White, S.D. M., Bianchi, S., 2004, MNRAS, 384, 964
- Mulchaey, J.S., & Zabludoff, A.I. 1998, ApJ, 496, 73
- Nusser, A., & Haehnelt, M. 1999, MNRAS, 303, 179
- Nusser, A. 2000, MNRAS, 317, 902
- Pando, J., Feng, L.L., Jamkhedkar, P., Zheng, W., Kirkman, D., Tytler, D., & Fang, L.Z. 2002, ApJ, 574, 575
- Pando, J., Feng, L.L., & Fang, L.Z. 2004, ApJS, 154, 475
- Pen, U.L. 1999, ApJ, 510, 1
- Polyakov, A.M. 1995, Phys. Rev. E, 52, 6183
- Raymond, J. C., & Smith, B. W. 1977, ApJS, 35, 419
- Ryu, D., et al. 1993, ApJ, 414, 1
- Seljak, U., & Zaldarriaga, M. 1996, ApJ, 469, 437
- Shandarin, S.F., & Zel'dovich, Y. B. 1989, Rev. Mod. Phys., 61, 185
- Shraiman, B.I., & Siggia, E.D. 2000, Nature, 405, 639
- Shu, C.W. 1998, in Advanced Numerical Approximation of Nonlinear Hyperbolic Equations, ed. A. Quarteroni (Berlin: Springer), 325

- Shu, C.W. 1999, Lecture Notes in Computational Science and Engineering, 9, 439.
- Sutherland, R.S. & Dopita, M. A., 1993, ApJS, 88, 253
- Shu, C.W. 2003, Int. J. Comput. Fluid Dyn., 17, 10
- Springel, V., Hernquist, L., 2002, MNRAS, 333, 649
- Takizawa, M. 1998, ApJ, 509, 579
- Theuns, T., et al. 1998, MNRAS, 301, 478
- Tozzi, P., & Norman, C. 2001, ApJ, 546, 63
- Valageas, P., & Silk, J. 1999, A&A, 350, 725
- Valageas, P., Schaeffer, R., & Silk, J. 2002, A&A, 388, 741
- Vergassola, M., Dubrulle, B., Frisch, U., & Noullez, A. 1994, A&A 289, 325
- Voit, G.M., et al, 2002, ApJ, 576, 601
- Worsley, M.A., et al. 2005, MNRAS, 357, 1281
- Wu, X.P., Xue, Y.J. & Fang, L.Z. 1999, ApJ, 524, 22
- Xu, W., Fang, L.Z., & Wu, X.P. 2000, ApJ, 532, 728
- Xu, W., Fang, L.Z., & Wu, X.P. 1998, ApJ, 508, 472
- Xue, Y.J., & Wu, X.P. 2000, ApJ, 538, 65
- Xue, Y.J., & Wu, X.P. 2003, ApJ, 584, 34
- Yang, X.H., Feng, L.L., Chu, Y.Q., & Fang, L.Z. 2001, ApJ, 560, 549
- Yoshida, N., Furlanetto, S.R., Hernquist, L., 2005, ApJ, 618, L91
- Yoshida, N., Sugiyama, N., Hernquist, L., 2003, MNRAS, 344, 481
- Zhang, P.J., & Pen, U.L. 2003, ApJ, 588, 704

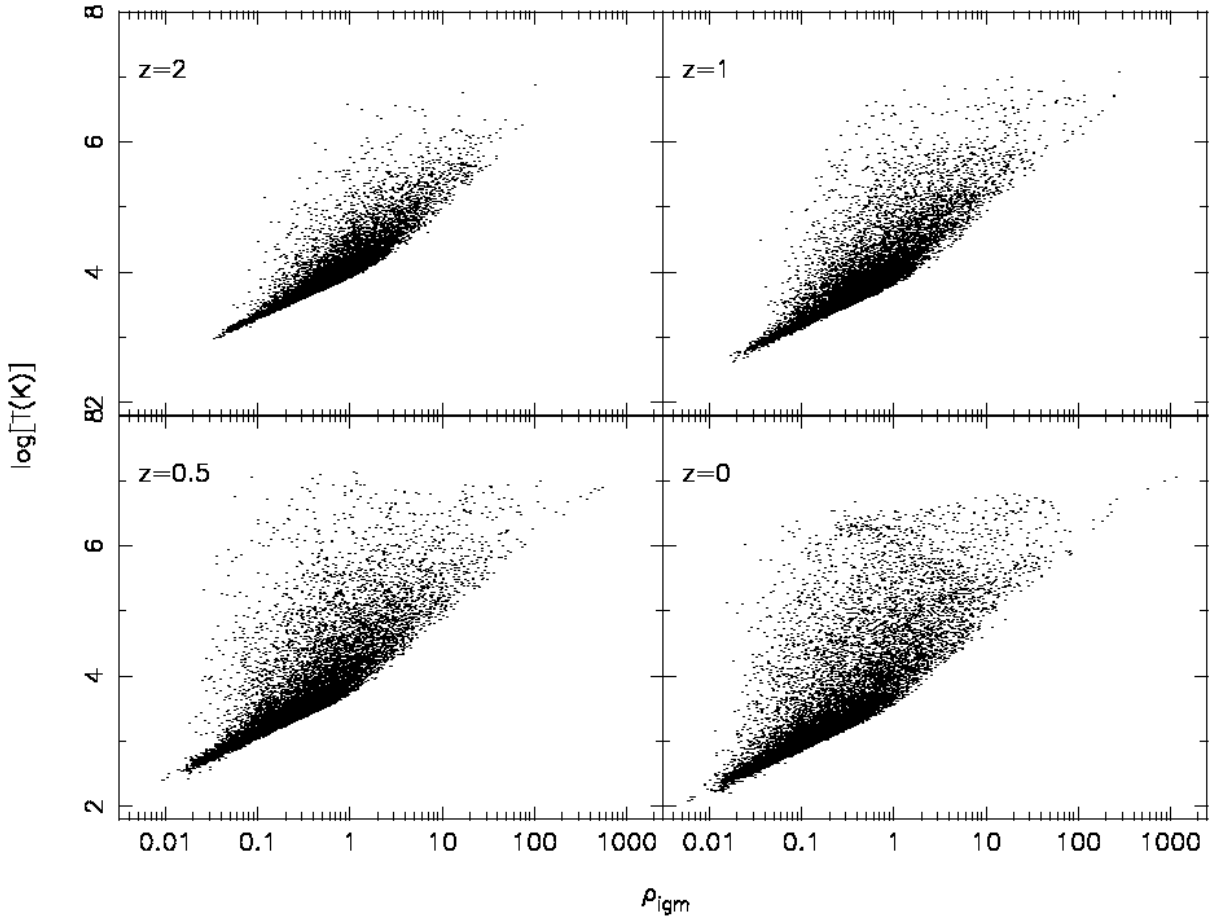


Fig. 1.— Temperature  $T$  vs. baryon density  $\rho_{\text{igm}}$  for sample C at redshifts 2, 1, 0.5, and 0, where  $\rho_{\text{igm}}$  is in units of the mean baryonic matter density  $\bar{\rho}_{\text{igm}}$ . Each panel contains 19,200 data points randomly selected from sample C.

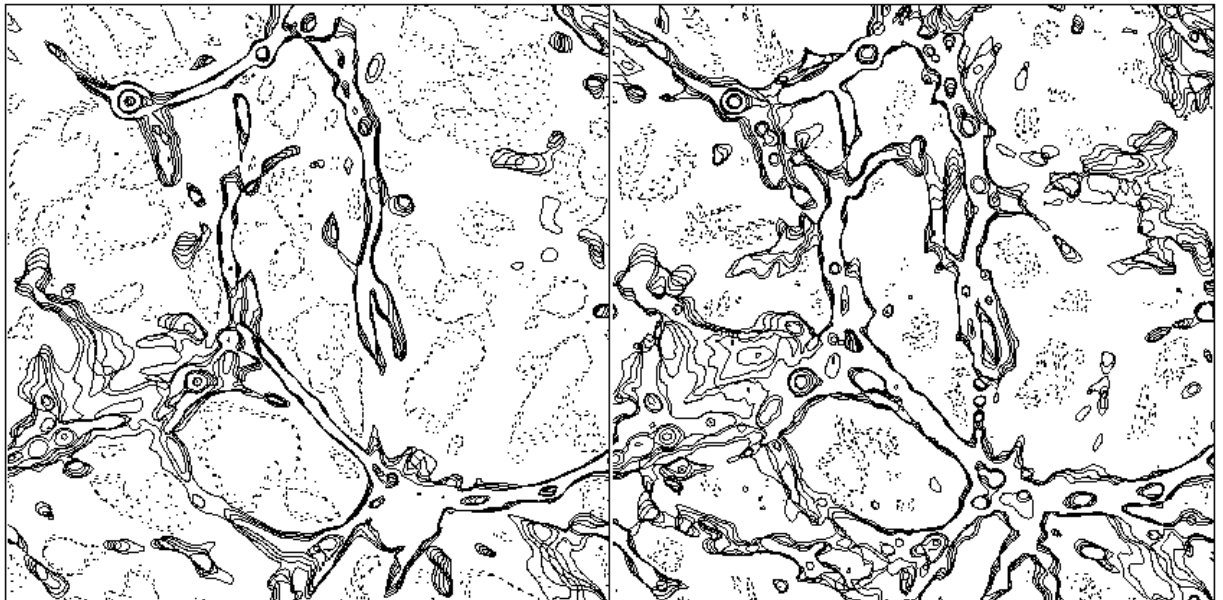


Fig. 2.— Density contour plots of dark matter (*left*) and baryonic gas (*right*) for a slice of  $0.26 h^{-1}$  Mpc thickness at  $z = 0$ . The solid contours encompass the over-dense regions with  $\rho = e^{i/2}$ ,  $i = 0, 1, 2, \dots$  ( $\bar{\rho}$  is normalized to 1), while the dotted lines represent the boundaries of the under-dense regions with  $\rho = e^{-i/2}$ ,  $i = 1, 2, \dots$

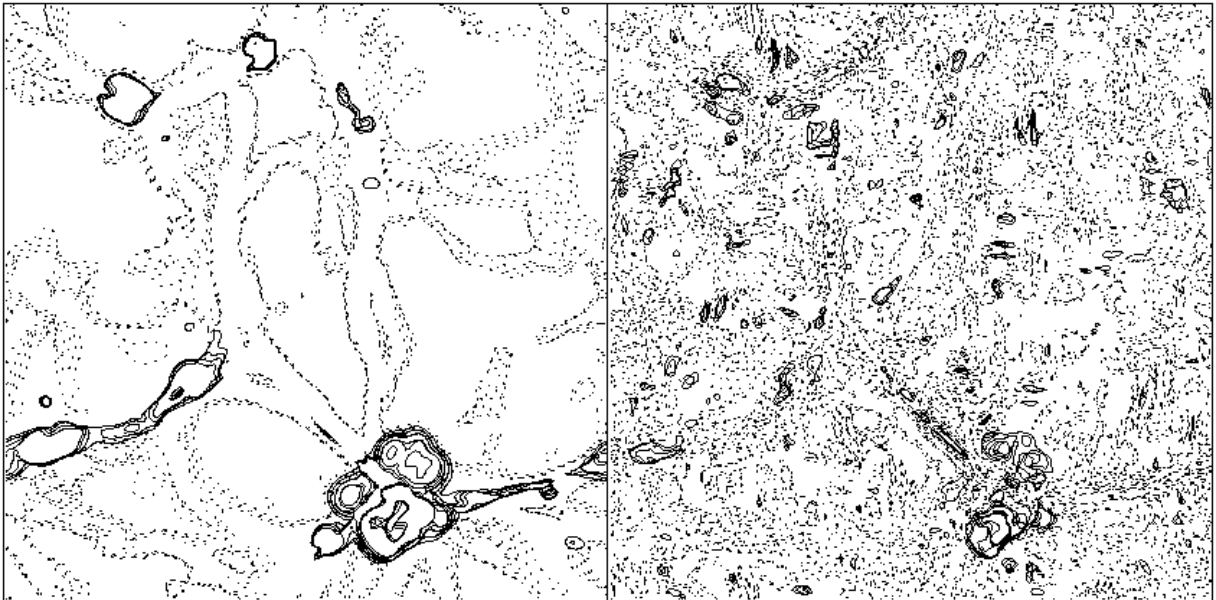


Fig. 3.— Contour plots of baryon to dark ratio  $\rho_{\text{igm}}/\rho_{\text{dm}}$  (left) and temperature  $T$  (right) for the same slice as in Figure 2. The solid contours represent, respectively, the regions with  $\rho_{\text{igm}}/\rho_{\text{dm}} = e^{i/3}, i = 0, 1, 2, \dots$ , and  $T = e^{i/2} \times 10^5 \text{ K}, i = 0, 1, 2, \dots$ , while the dotted lines represent  $\rho_{\text{igm}}/\rho_{\text{dm}} = e^{-i/3}, i = 1, 2, \dots$ , and  $T = e^{-i/2} \times 10^5 \text{ K}, i = 1, 2, \dots$ , regions.

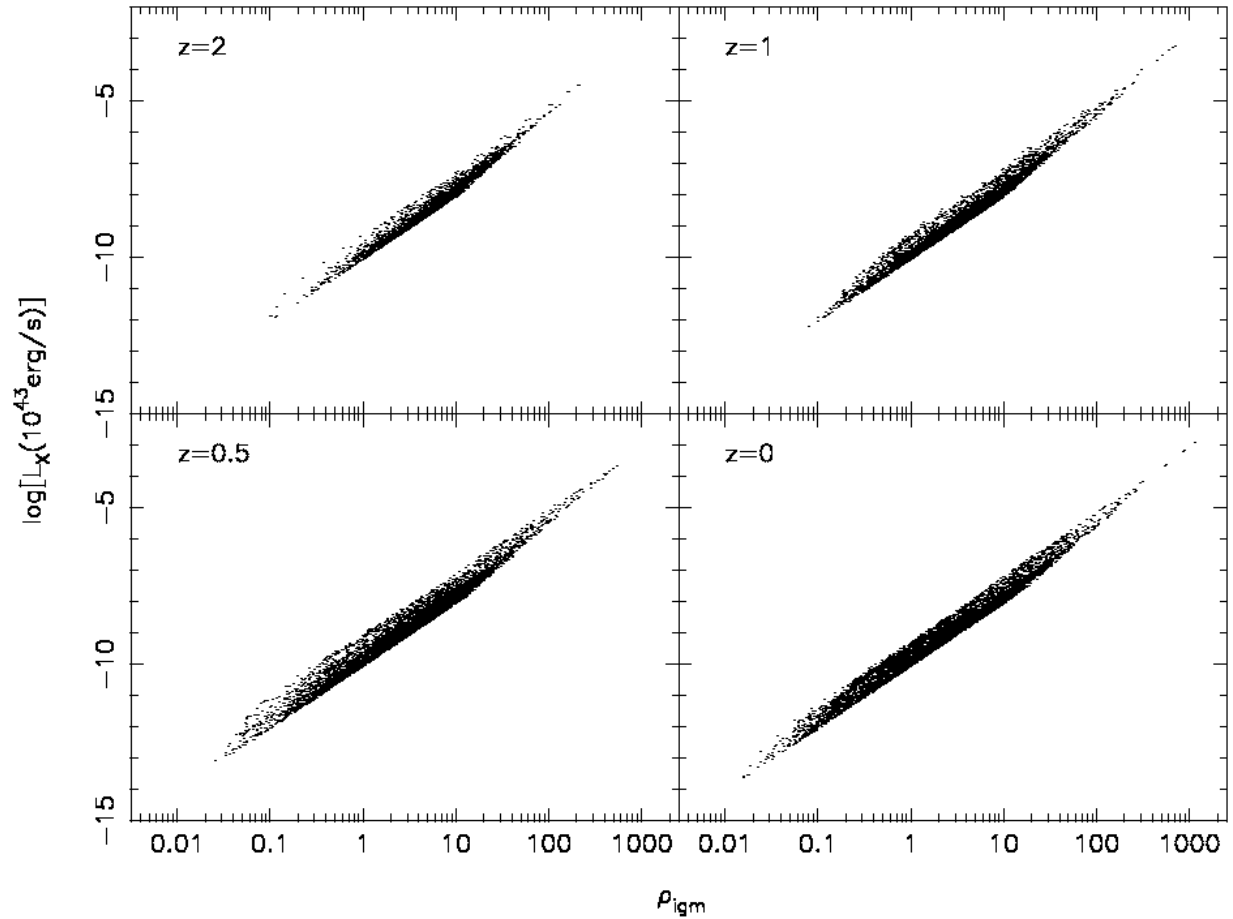


Fig. 4.— X-ray luminosity  $L_x$  vs. baryon density  $\rho_{\text{igm}}$  for sample C, where  $\rho_{\text{igm}}$  is in units of the mean baryonic matter density  $\bar{\rho}_{\text{igm}}$ . The panels at  $z=0.0$ ,  $0.5$ ,  $1.0$ , and  $2$  show, respectively, 9931, 9119, 7314, and 4864 data points randomly selected from sample C in each redshift, and with temperature  $T > 10^5$  K.

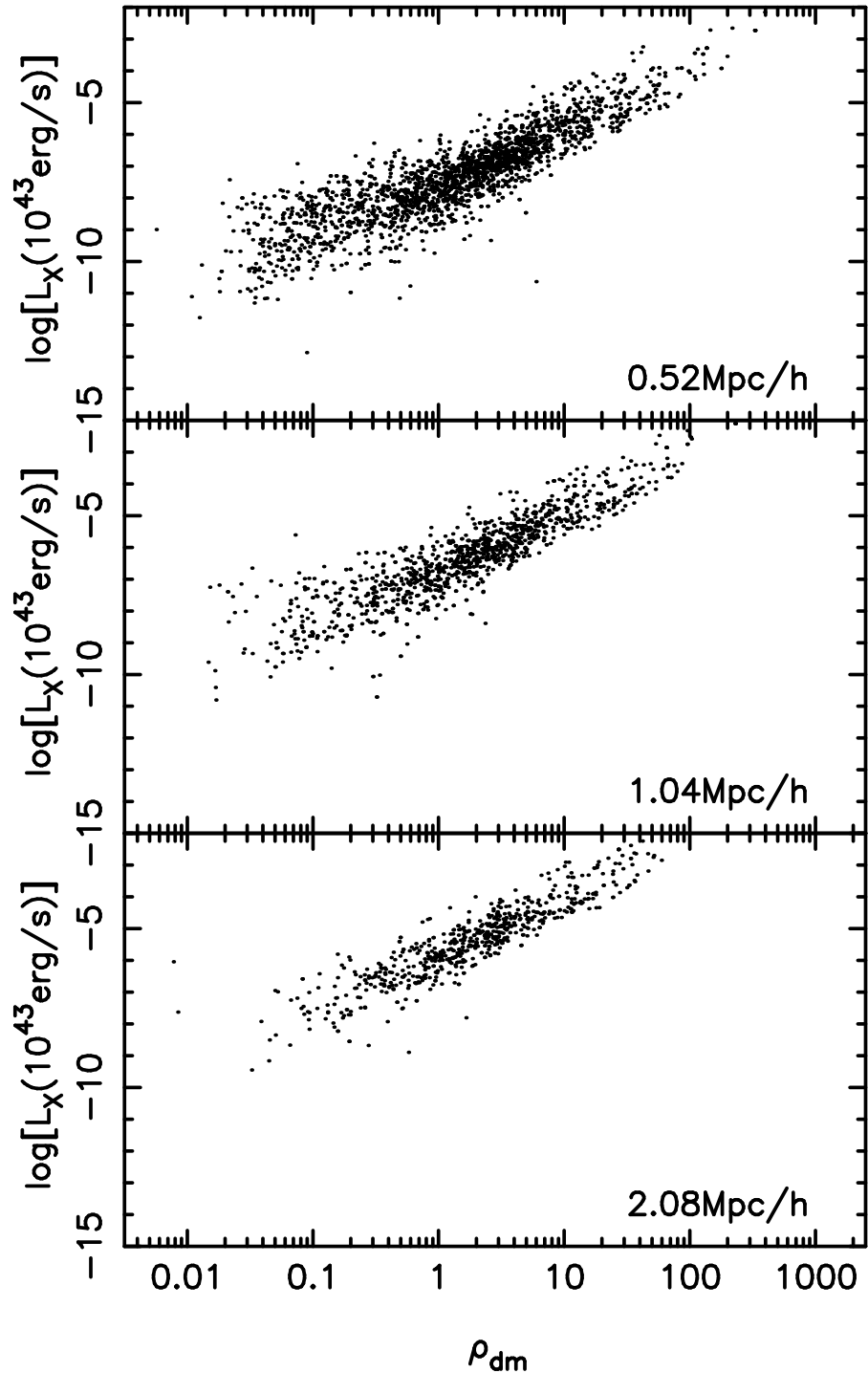


Fig. 5.— X-ray luminosity  $L_x$  vs. dark matter density  $\rho_{\text{dm}}$  for sample C at redshift  $z = 0$  and decomposed on scales of  $0.52$ ,  $1.04$ , and  $2.08 h^{-1} \text{ Mpc}$ . Here  $\rho_{\text{dm}}$  is in units of the mean dark matter density  $\bar{\rho}_{\text{dm}}$ .

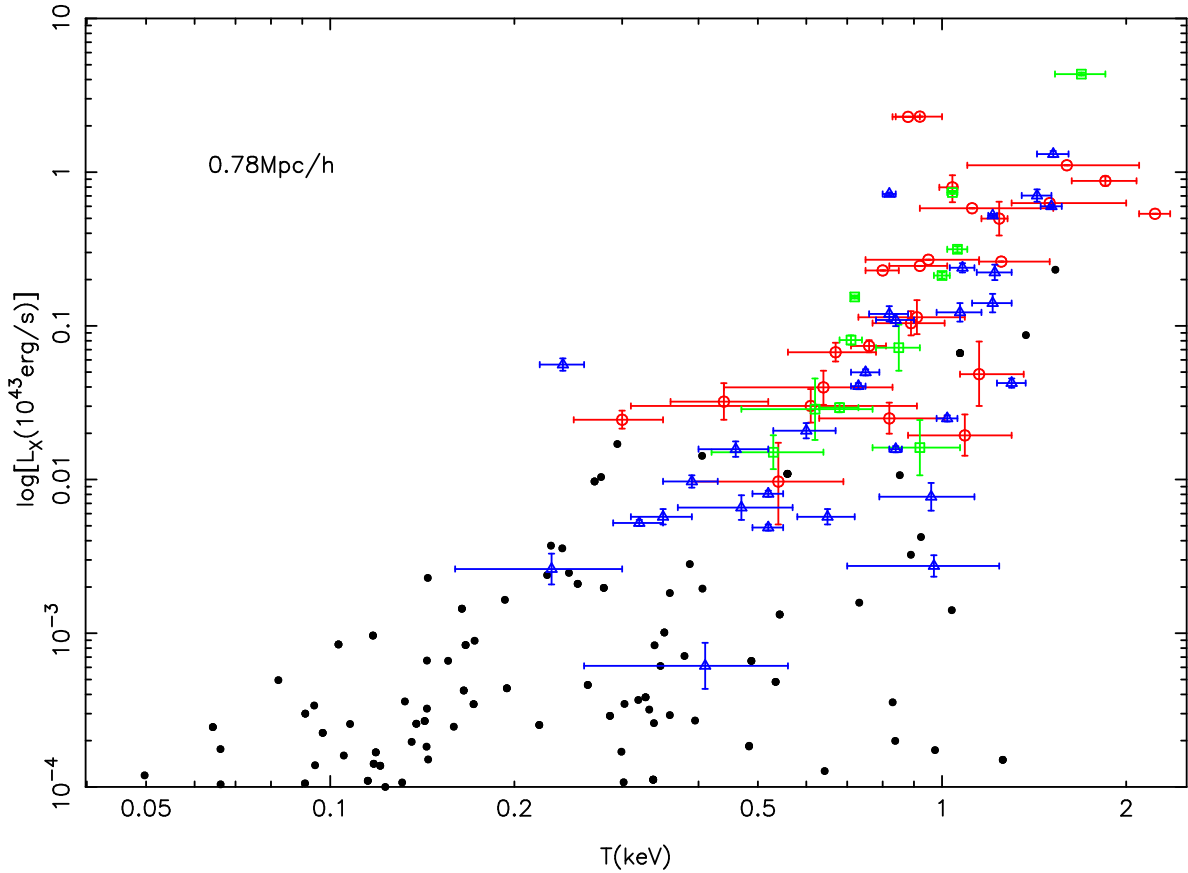


Fig. 6.— X-ray luminosity  $L_x$  vs. temperature  $T$  for samples A at redshift  $z = 0$  with the DWT decomposition on scales of  $0.78 h^{-1}$  Mpc. The observed data are adapted from Helsdson & Ponman (2000; *squares*), Xue & Wu (2000; *circles*) and Croston et al (2005; *triangles*).

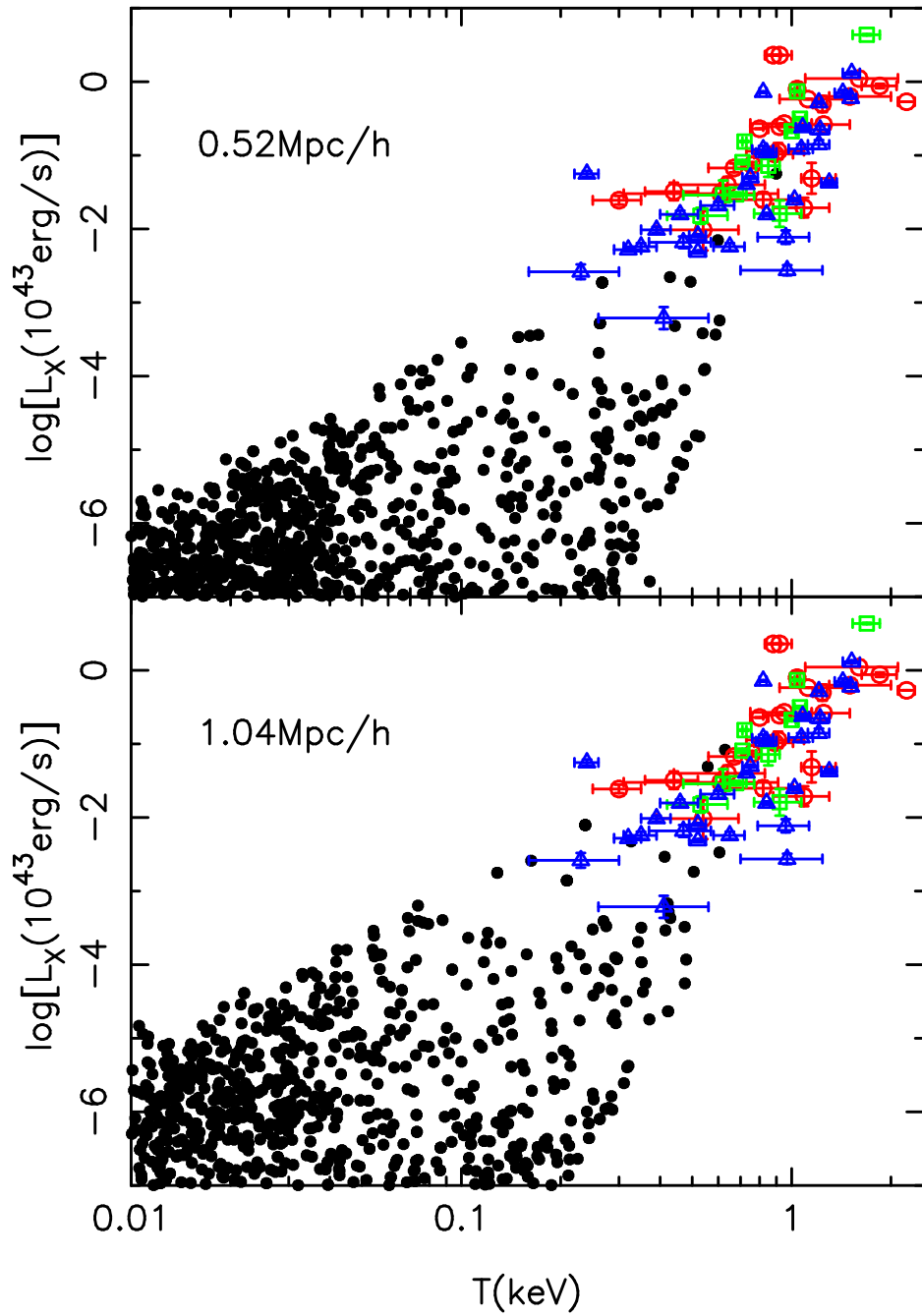


Fig. 7.— Same as Fig.6, but for sample C at redshift  $z = 0$  with the DWT decomposition on scales of 0.52 (top) and  $1.04 h^{-1} \text{ Mpc}$  (bottom).

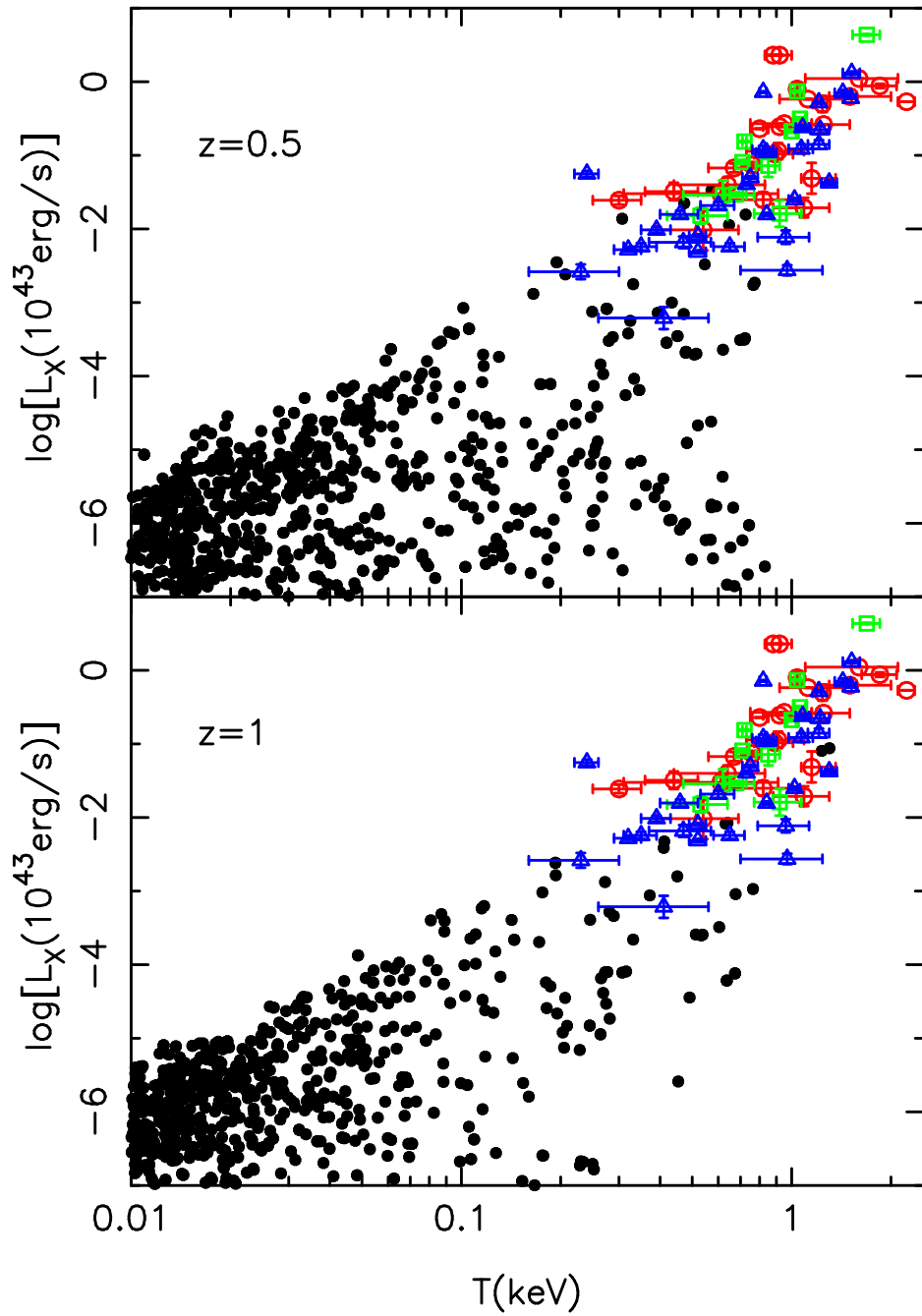


Fig. 8.— Same as Fig. 7, but for redshift  $z = 0.5$  (top) and  $z = 1$  (bottom). The physical scale of the DWT decomposition is  $0.69 h^{-1} \text{Mpc}$ .

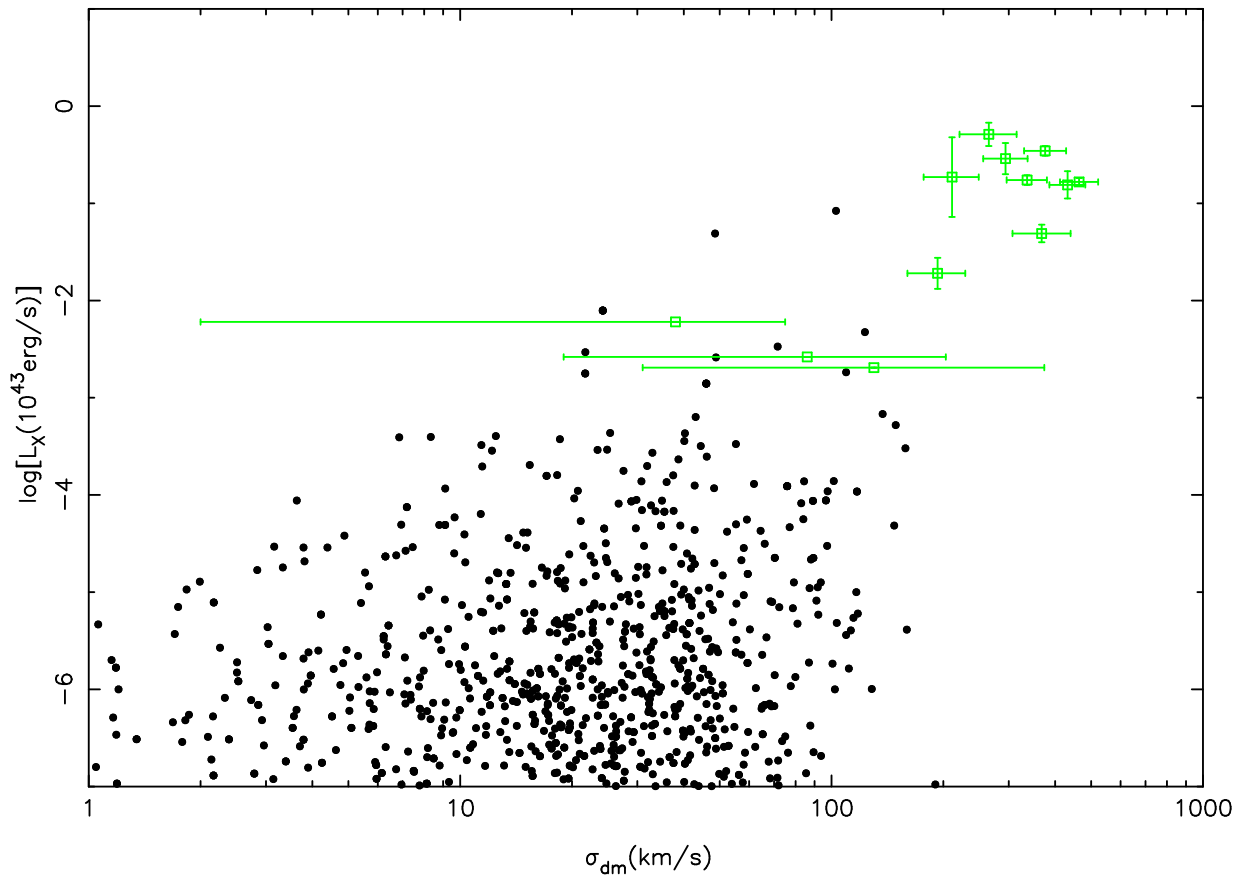


Fig. 9.— X-ray luminosity  $L_x$  vs. velocity dispersion of dark matter  $\sigma_{\text{dm}}$  for sample C at redshift  $z = 0$  with the DWT decomposition on scales of  $1.04 h^{-1}$  Mpc. The observed data are adapted from Mulchaey & Zabludoff(1998).

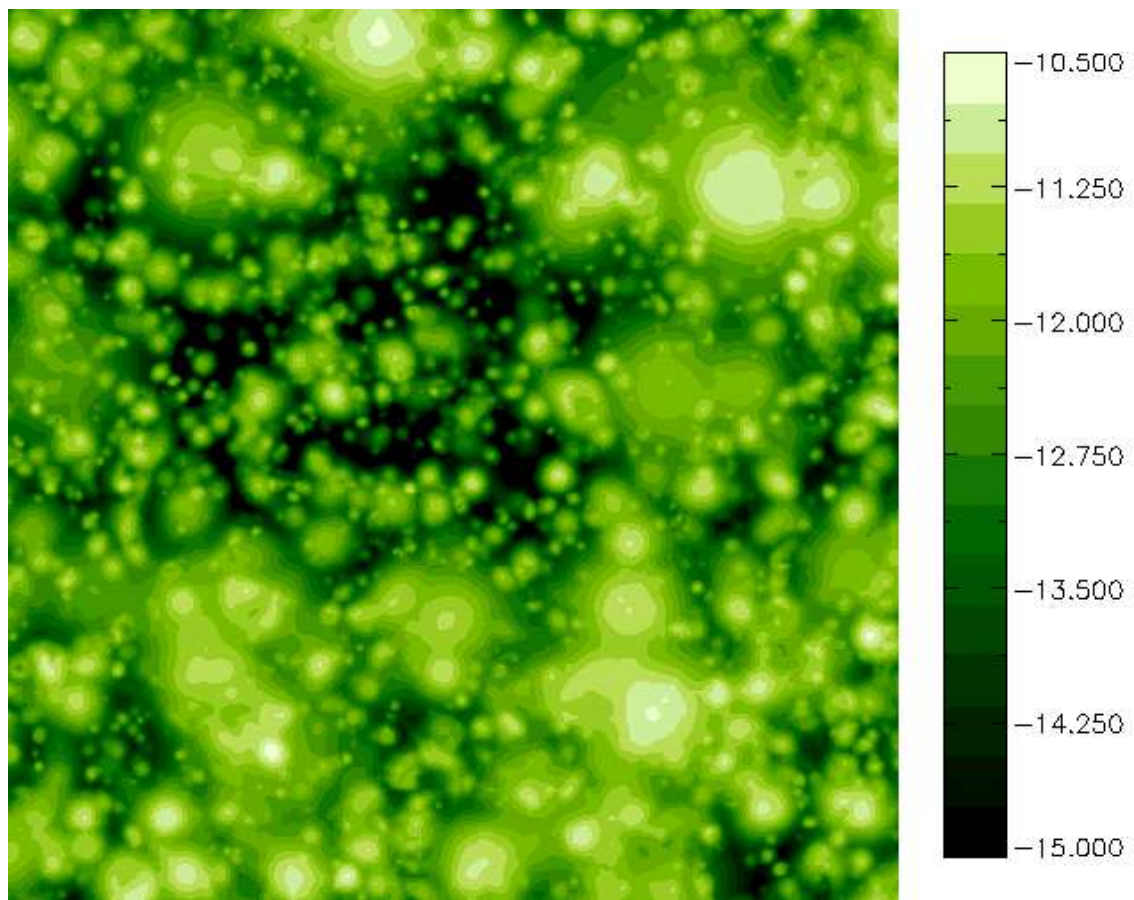


Fig. 10.— A  $1^\circ \times 1^\circ$  map of X-ray intensity in soft 0.5-2 keV band for simulation sample A.

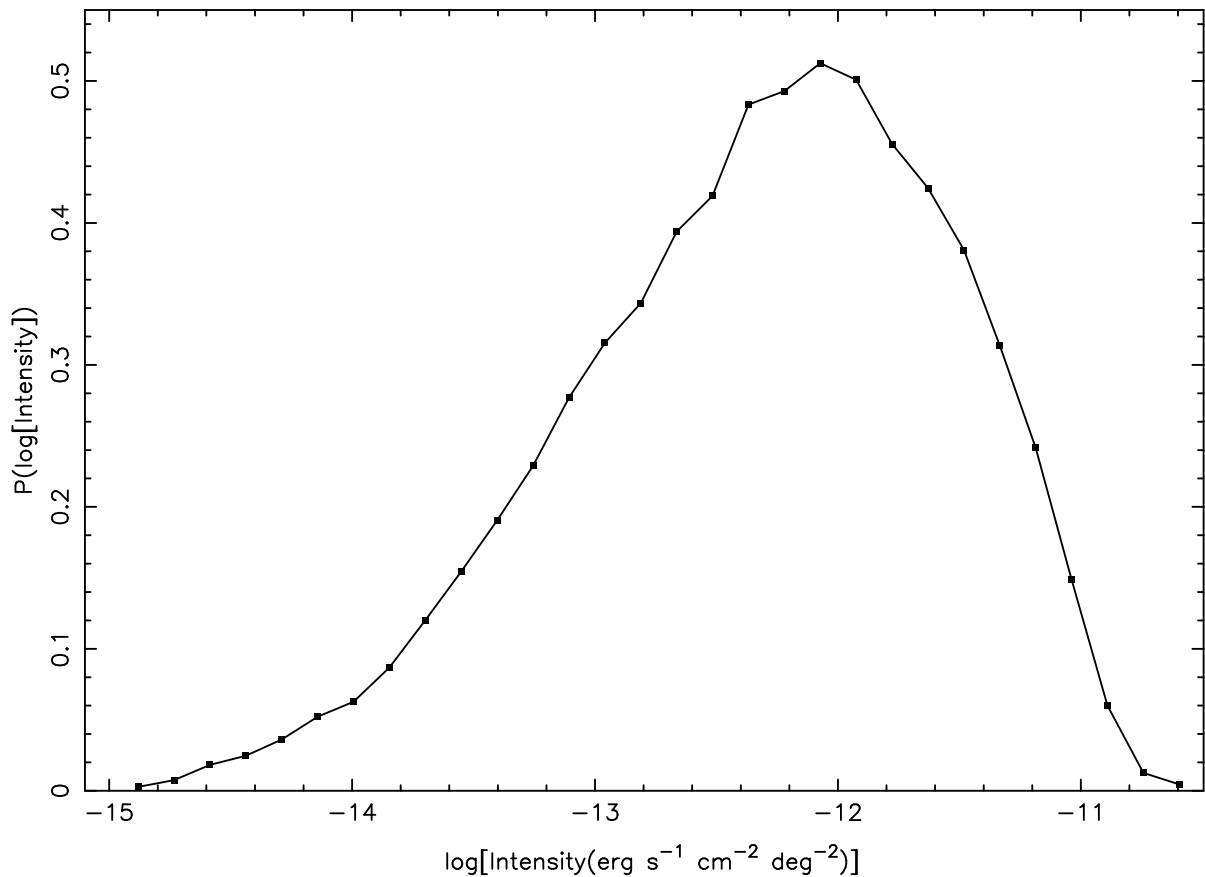


Fig. 11.— Probability distribution function of X-ray intensity in the 0.5-2 keV band for the same samples as in Fig.10.

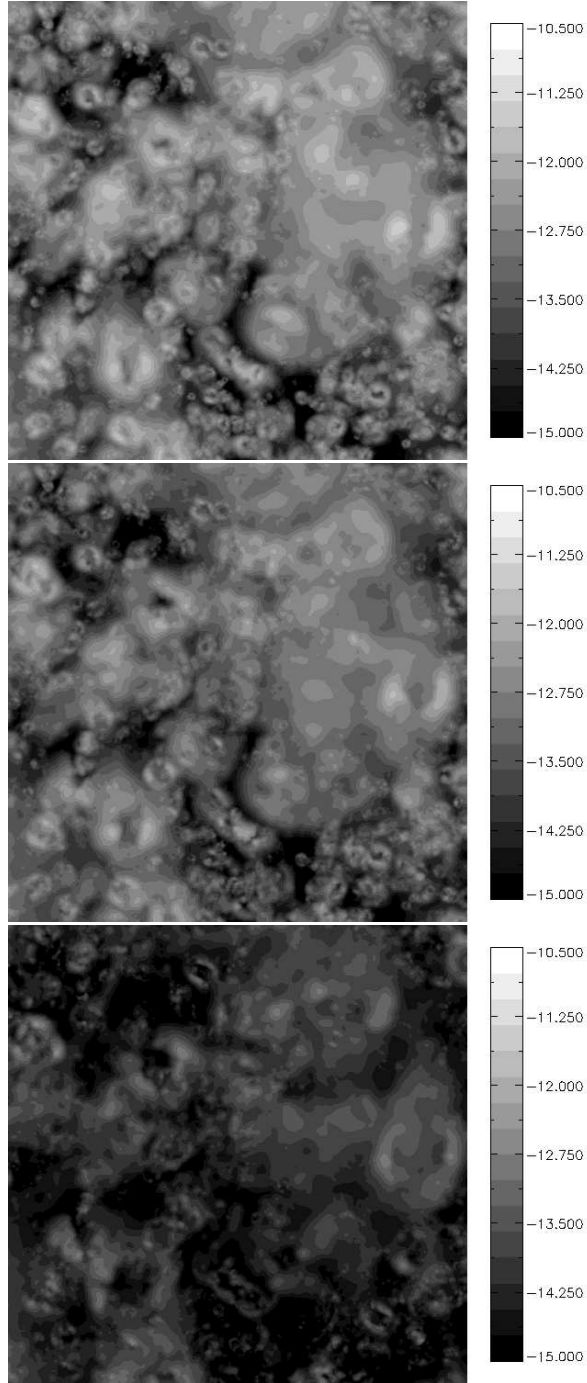


Fig. 12.— Same as Fig.10, but for baryonic clouds located in regions with dark matter density  $\rho_{\text{dm}} < 100$  (*top*), 50 (*middle*) and 10 (*bottom*), where  $\rho_{\text{dm}}$  is in units of the mean dark matter density  $\bar{\rho}_{\text{dm}}$ .

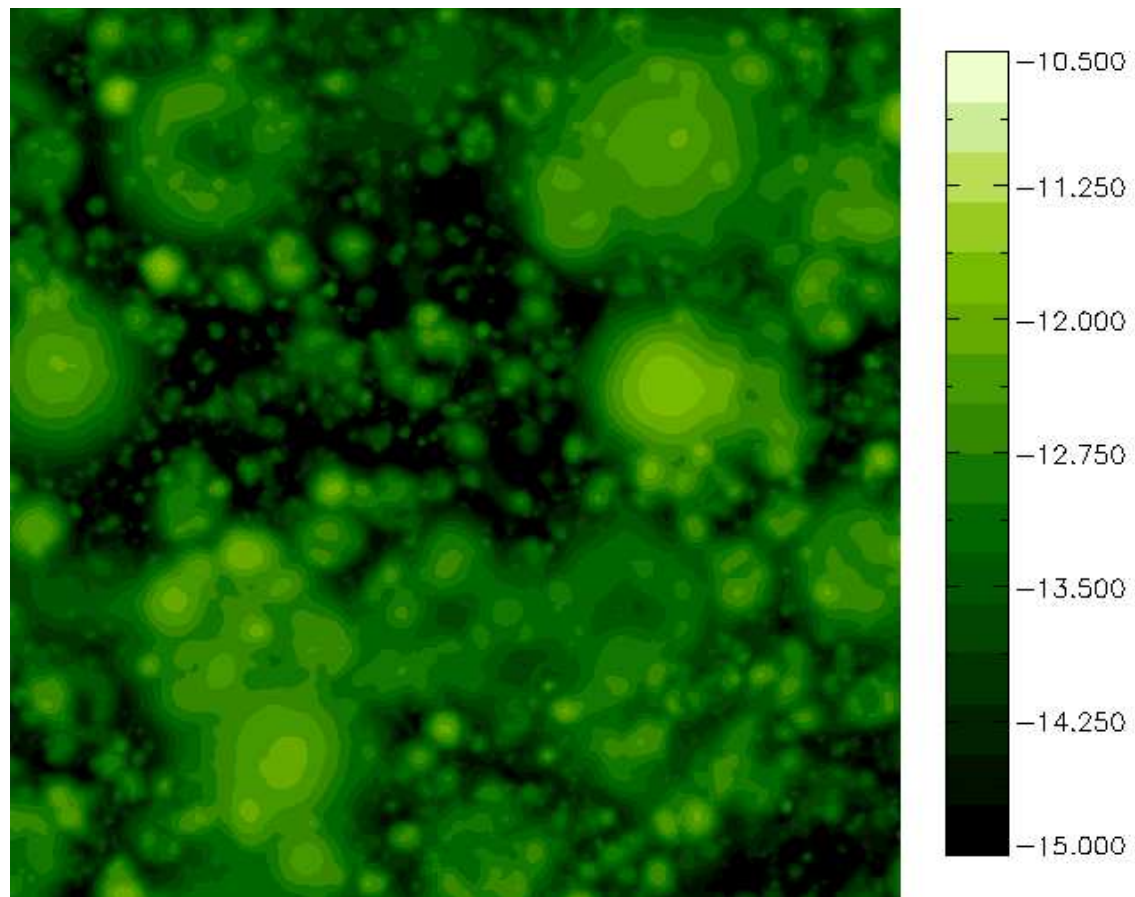


Fig. 13.— Same as Fig.10, but for baryonic clouds with temperature in the range  $10^5 < T < 10^{6.5}$  K.

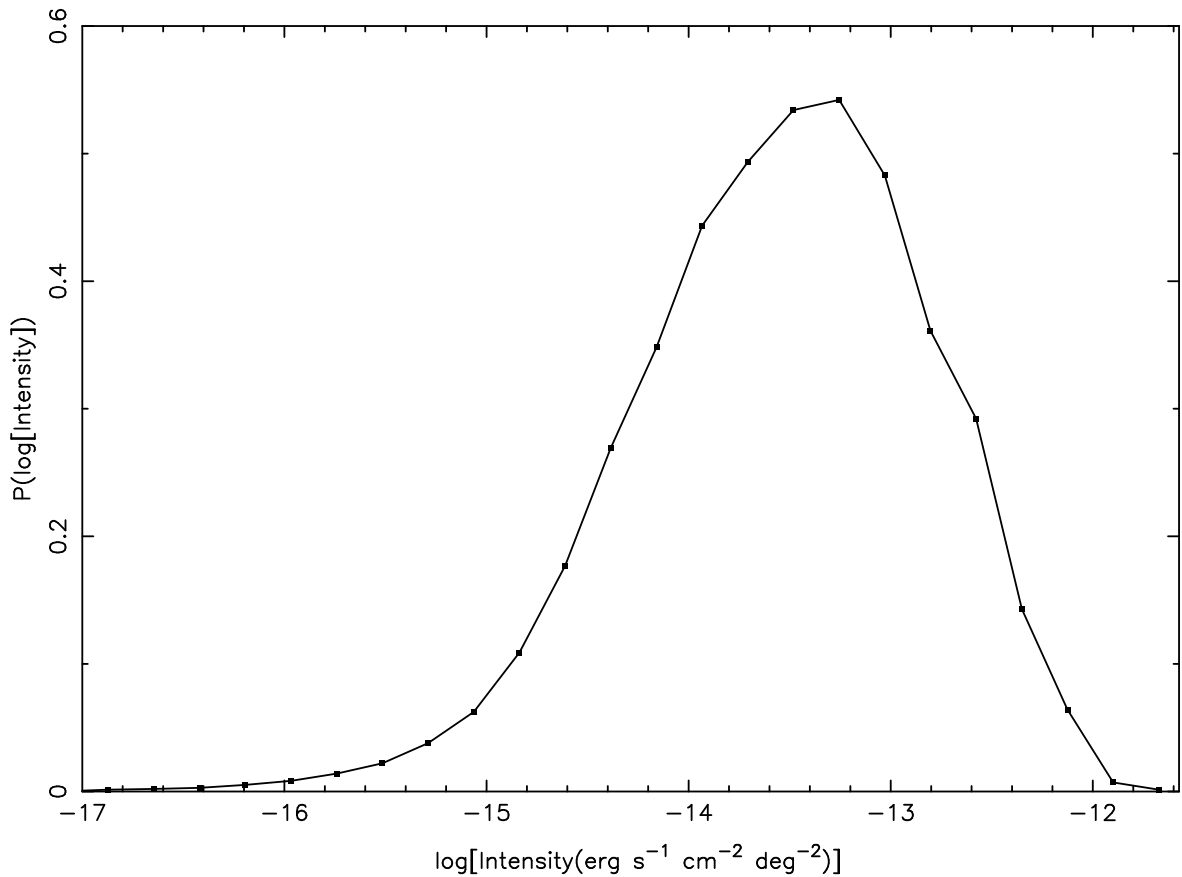


Fig. 14.— Same as Fig.11, but for the x-ray emission from clouds with temperature in range  $10^5 < T < 10^{6.5}\text{K}$  (the same samples as in Fig.13).